

Enhanced Polymer Crystallinity in Mixed Matrix Membranes Induced by Metal–Organic Framework Nanosheets for Efficient CO₂ Capture

*Youdong Cheng,[†] Sérgio R. Tavares,[‡] Cara M. Doherty,[§] Yunpan Ying,[†] Erik Sarnello,^{||}
Guillaume Maurin,[‡] Matthew R. Hill,^{§,⊥} Tao Li,^{||,#} and Dan Zhao^{*,†}*

[†] Department of Chemical and Biomolecular Engineering, National University of Singapore, 4
Engineering Drive 4, Singapore 117585

[‡] Institut Charles Gerhardt Montpellier, Université de Montpellier, Place E. Bataillon,
Montpellier Cedex 05, 34095, France

[§] CSIRO Manufacturing, Private Bag 10, Clayton South, Victoria 3169, Australia

^{||} Department of Chemistry and Biochemistry, Northern Illinois University, DeKalb, IL 60115,
USA

[⊥] Department of Chemical Engineering, Monash University, Clayton, Victoria 3800, Australia

[#] X-Ray Science Division, Advanced Photon Source, Argonne National Laboratory, Argonne, IL
60439, USA

KEYWORDS

CO₂ capture, mixed matrix membranes, metal–organic framework nanosheets, polymer
crystallinity, anti-aging

ABSTRACT

The design and fabrication of novel mixed matrix membranes (MMMs) with simultaneously enhanced gas permeability and selectivity are highly sought for the industrial deployment of membrane technology for large-scale CO₂ capture and storage. Conventional isotropic bulky particle fillers often exhibit limited interfacial compatibility that eventually leads to significant selectivity loss in MMMs. Here we report the incorporation of chemically stable metal–organic framework (MOF) nanosheets into a highly permeable polymer matrix to prepare defect-free MMMs. MOF nanosheets are homogeneously dispersed within the polymer matrix owing to their high aspect ratios that improve the polymer-filler integration. The strong hydrogen bonding and π – π interactions between the two components not only enhance the interfacial compatibility, but also favor the efficient polymer chain packing along the surface of MOF nanosheets, leading to enhanced polymer crystallinity as well as size-sieving capability of the membranes. The as-prepared MMMs demonstrate high CO₂-selective separation performance, good anti-pressure and anti-aging abilities, thus offering new opportunities in developing advanced membranes for industrial gas separation applications.

INTRODUCTION

The soaring increase of CO₂ emission caused by anthropological activities has aroused great concerns over the past decades owing to its profound influence on the sustainability of global environment as well as human society. CO₂ capture and storage (CCS), a process aimed at reducing CO₂ emission by selective capture and long-term storage of combustion-generated CO₂ in suitable places, has been widely recognized as a key component of a great number of national, regional, and global scenarios for CO₂ emission reduction.¹ Among various technologies for CCS, membrane technology has gained great interest owing to its high energy efficiency, low capital investment, as well as continuous and simple operation. Nevertheless, current commercial membranes constructed from low-permeable polymers are not so economically attractive when processing massive volumes of gas mixtures in CCS owing to the demand of large membrane areas. Moreover, a trade-off effect between permeability and selectivity, known as Robeson upper bound,^{2,3} commonly exists in conventional polymeric materials, further impeding the industrial deployment of membrane technology for CCS.

A facile yet effective strategy to boost the current membrane separation performance is the design and fabrication of a class of advanced membranes, named mixed matrix membranes (MMMs), by dispersing highly selective and permeable microporous organic/inorganic fillers into a processable polymer matrix, where both phases work synergistically to offer high-performance membranes in a scalable approach suitable for industrial gas separations. A wide range of materials have been explored as fillers, including zeolites,⁴ silicas,⁵ metal oxides,⁶ graphene oxide,⁷ metal-organic frameworks (MOFs),⁸ etc. Among them, MOFs, a class of porous crystalline materials consisting of inorganic nodes and organic linkers, have aroused great interest in MMMs owing to their high surface area, adjustable pore architectures, and rich chemical versatility.⁹ Up till now,

considerable efforts have been devoted to exploring the promising separation performance of MOFs in MMMs. However, traditional MOF synthesis commonly produces isotropic bulky crystals that undermine their interfacial interactions with the polymer matrix, easily leading to phase segregation in MMMs. Moreover, it is highly desirable to improve the size-sieving capability of the polymer matrix to further enhance the gas pair selectivity, which has rarely been realized in MMMs owing to the lack of a delicate design on strong polymer-fillers interactions. As a result, the ultimate goal of fabricating promising MMMs for industrial CCS still remains as a formidable challenge.

Herein, we report the design and characterization of robust MMMs composed of porous NUS-8 (NUS stands for National University of Singapore) MOF nanosheets as fillers and polymer of intrinsic microporosity 1 (PIM-1) as the polymer matrix for efficient CO₂ capture. NUS-8 consists of zirconium clusters and 1,3,5-benzenetribenzoate (BTB) as the organic linker (Figure 1), exhibiting extraordinarily high chemical stability towards boiling water and even acidic solutions.¹⁰ Their facile and scalable synthesis in nanosheet morphology via a modulated hydrothermal approach paves the way towards prospective industrial applications. Besides, their unidirectional diamond shaped channels with an internal diameter of 6 Å are suitable for the fast permeation of light gas molecules. PIM-1 exhibits ultrahigh gas permeability due to its large fractional free volume originating from its rigid and contorted structure. Although PIM-1 is notoriously known for its glassy nature that prevents its effective interaction with conventional bulky fillers, the high aspect ratio of NUS-8 nanosheets can maximize their contacting area with PIM-1 matrix. Coupled with hydrogen bonding and π - π interactions between these two phases, adding NUS-8 nanosheets as fillers can lead to enhanced PIM-1 crystallinity as well as size-sieving capability of the resultant MMMs. The MMM with only 2 wt% of NUS-8 nanosheets exhibits a

superior selectivity in CO₂ capture (30.1 for CO₂/CH₄ and 26.8 for CO₂/N₂) accompanied by a two-fold increase in CO₂ permeability compared with that of pure PIM-1 membrane, largely surpassing the 2008 Robeson upper bound limit.³ Moreover, the addition of NUS-8 nanosheets helps to freeze the membrane initial fractional free volume in place and to effectively retard the membrane aging process, offering new opportunities for the design and fabrication of novel membranes for efficient CO₂ capture.

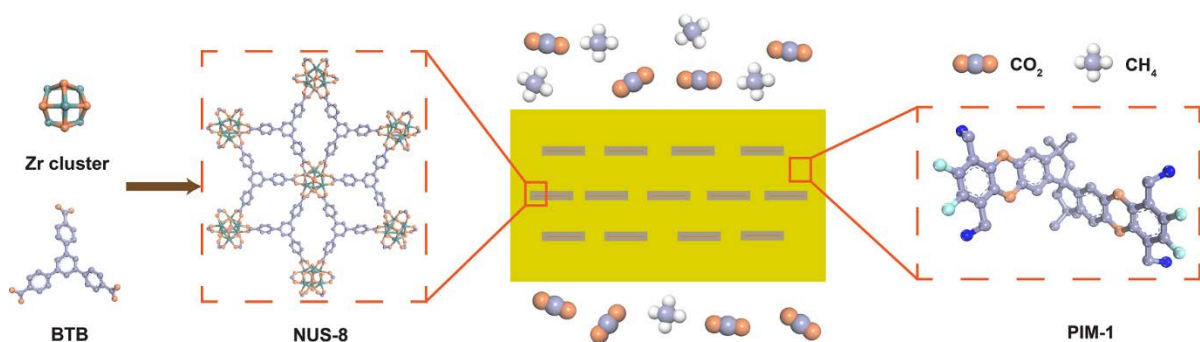


Figure 1. Schematic illustration of the synthesis of NUS-8 nanosheets from the building blocks of Zr cluster and BTB ligand (left); gas separation process in NUS-8/PIM-1 MMMs (middle); chemical structure of PIM-1 polymer (right).

EXPERIMENTAL SECTION

Materials

All the chemicals and reagents are commercially available and used as received without purification. Anhydrous potassium carbonate (K₂CO₃, 99.5%), zirconium(IV) chloride (ZrCl₄, 99.99%), 1,3,5-benzenetribenzoic acid (H₃BTB, 98%), acetic acid (99%), tetrafluoroterephthalonitrile (TFTPN, 99%) and 5,5',6,6'-tetrahydroxy-3,3,3',3'-tetramethyl-1,1'-spirobisindane (TTSBI, 97%) were purchased from Sigma-Aldrich. Methanol (99.8%), N,N-

dimethylformamide (DMF, HPLC grade), tetrahydrofuran (THF, HPLC grade) and chloroform (99.8%) were obtained from Fisher Scientific.

Synthesis of NUS-8 nanosheets

H₃BTB (2.2 g) and ZrCl₄ (1.2 g) were mixed in 50 mL of mixed solvent containing deionized water and acetic acid (v/v = 3/2) in a 100 mL round flask. After reacting at 120 °C for 24 h under vigorous stirring, the produced white precipitate was recovered by centrifuge and repeatedly washed with methanol and deionized water. To completely remove the residual ligand and metal salt, the product was immersed in methanol for 3 days, during which time the extract was decanted and fresh methanol was added every half a day. After removal of methanol by decanting during the last solvent exchange, the sample was dried under a dynamic vacuum at 120 °C for 24 h to yield the final product (yield: 68% based on the total mass of reactants).

Synthesis of PIM-1

TTSBI (10.2 g), TFTPn (6 g) and K₂CO₃ (8.3 g) were mixed in 200 mL of DMF. The mixture solution was stirred under nitrogen atmosphere at 60 °C for 48 h. After cooling to room temperature, the solution was poured into 300 mL of deionized water. The precipitate was collected by filtration and repeatedly washed with deionized water and methanol. The obtained PIM-1 polymer was purified by dissolving in chloroform and re-precipitation from methanol, filtered and dried under a dynamic vacuum at 120 °C for 24 h (yield: 91% based on the total mass of reactants). The molecular weight distribution of the synthesized PIM-1 was determined by gel permeation chromatography (GPC) using polystyrene standards as comparisons, giving an average molecular weight of Mn = 58606; Mw = 188746, with the polydispersity (PDI) = 3.22.

Preparation of NUS-8/PIM-1 MMMs

The NUS-8/PIM-1 MMMs were prepared by physical blending. PIM-1 was completely dissolved in THF to form a stock solution (6 wt%), and NUS-8 nanosheets were sonicated in THF for 2 h. Then PIM-1 stock solution was filtrated through the PTFE syringe filter (0.45 μm) into certain amounts of NUS-8 nanosheet dispersion. The resulting casting solution was stirred overnight and then poured into glass petri dishes, followed by a slow evaporation over two days at ambient temperature. The as-prepared membranes were collected from the glass petri dishes and dried under vacuum at 100 $^{\circ}\text{C}$ prior to gas permeation and structure characterization. MMMs were prepared with loadings of NUS-8 nanosheets at 0.5, 1, 2 and 5 wt%. The thickness of the final pure and composite membranes varied within the range of 50–80 μm , as measured by a digital micrometer.

Characterization

The phase purity and crystallinity of NUS-8 nanosheets and all membranes were confirmed by X-ray diffraction (XRD). The XRD patterns were collected on a Rigaku MiniFlex X-ray diffractometer at a scan rate of 0.02 deg s^{-1} . The morphologies of NUS-8 nanosheets and all membranes were characterized by a field emission scanning electron microscope (FESEM, FEI Quanta 600), and the corresponding elemental mapping was conducted using an energy dispersive spectrometer (EDS, Oxford Instruments, 80 mm^2 detector). The dimension of NUS-8 nanosheets was characterized by tapping mode atomic force microscopy (AFM, Bruker) and transmission electron microscopy (TEM, JEOL-JEM 2010F). The gas sorption isotherms of N_2 , CO_2 and CH_4 were obtained using a Micromeritics ASAP 2020 physisorption analyzer. Before each measurement, the sample (~ 50 mg) was degassed under reduced pressure ($< 10^{-2}$ Pa) at 120 $^{\circ}\text{C}$ for 12 h. Fourier transform infrared spectroscopy (FTIR) spectra were collected with a Bio-Rad FTS 3500 spectrometer under the attenuated total reflection (ATR) mode. Thermogravimetric

analyses (TGA) were performed in air atmosphere using Shimadzu DTG-60AH. Nano-indentation testing was performed to determine the Young's modulus of all as-prepared membranes using the contact mode AFM with a diamond tip (PDNISP). The deflection sensitivity of the cantilever is 221 nm V^{-1} with the spring constant at 227 N m^{-1} . Twenty points were obtained from each sample at different locations, and the average data were calculated on the basis of the measured values of three different samples. Viscosity measurements were performed in pure THF and THF solutions containing PIM-1, PIM-1/TiO₂, PIM-1 UiO-66-NH₂, or PIM-1/NUS-8. The weight percent of PIM-1 in THF was kept at 6 wt%, and the filler loading is 2 wt% based on the total weight of PIM-1 and the filler. Small angle X-ray scattering (SAXS) experiments were performed at the 12-ID-C station at Advanced Photon Source of Argonne National Laboratory (Argonne, Illinois, USA). Data were collected with an X-ray energy source of 13.3 keV with a sample-to-detector distance of 2 m. A PILATUS 2M detector was used with a typical exposure time of 0.1 s for each sample.

Gas permeation

Mixed gas separation tests for these membranes were operated with the home-built Wicke-Kallenbach gas permeation apparatus.¹¹ All membranes were sealed with a high temperature aluminum gasket coated with silicone rubber pad. Equal molar mixture of CO₂/CH₄ or CO₂/N₂ was used as the feed at a constant flow rate of 25 mL min^{-1} (Brooks Instrument). The concentration polarization effect in the permeate side was eliminated by sweeping argon at a volumetric flow rate of 50 mL min^{-1} . Gas chromatograph (Shimadzu GC-2014) was adopted to analyze the compositions of permeate side gases. Steady state was achieved when the compositions of permeate side gases did not shift with time and all permeation data were collected at the steady state. All membranes were repeated at least three times to ensure their stability. The gas permeability (P_i , Barrer, $1 \text{ Barrer} = 10^{-10} \text{ cm}^3 \text{ (STP) cm cm}^{-2} \text{ s}^{-1} \text{ cmHg}^{-1}$) is defined by Eq. (1),

$$P_i = \frac{Q_i l}{A \Delta p_i} \quad (1)$$

where Q_i refers to the gas volume flow rate ($\text{cm}^3 \text{ s}^{-1}$, STP), l refers to membrane thickness (μm), A refers to the effective membrane area (cm^2), Δp_i refers to partial pressure difference across the membrane (cmHg). The mixed gas selectivity (α_{ij}) is calculated by Eq. (2),

$$\alpha_{ij} = \frac{y_i/y_j}{x_i/x_j} \quad (2)$$

where x_i/x_j and y_i/y_j represents the molar fraction of i/j in the feed and permeate side, respectively.

Molecular dynamics (MD) simulations

As a preliminary step, the NUS-8 structure was first geometry-optimized at the DFT level and a microscopic model of the PIM-1 was created using force-field based MD simulations. The interface was finally modelled by means of a methodology previously developed by some of us.¹² The MOF and polymer components were brought into contact in a simulation box of $40.6 \times 67.27 \times 160 \text{ \AA}^3$ dimension. This composite system was equilibrated by several MD simulations in the NVT and in the NP_nT ensemble, where P_n corresponds to the pressure component in the z direction, the direction normal to the interface. The MOF/polymer interactions were treated using the sum of a Lennard-Jones (LJ) potential term and a coulombic contribution. Each atom of NUS-8 and PIM-1 was considered as a single charged LJ site with LJ potential parameters and charges described in the Supporting Information. After this equilibration step, data were collected from four statistically independent simulations to analyze the properties of the interfaces in terms of surface coverage, atomic density profile and interactions between the MOF and the polymer.

RESULTS AND DISCUSSION

Synthesis and characterization of NUS-8 nanosheets

MOF nanosheets can be readily obtained by top-down strategies that involve the disintegration of bulky MOF crystals into single- or multi-layered structures with external energy input, including mechanical exfoliation,¹³ liquid-assisted sonication¹⁴ and freeze-thaw-induced delamination.¹⁵ However, these top-down exfoliation processes may either lead to the severe breakage of large MOF nanosheets into small fragments, or result in low exfoliation yields (< 5%), or sometimes even both. On the contrary, the bottom-up strategies that produce MOF nanosheets directly from building blocks can be promising alternatives owing to their easy, fast, and massive production processes.¹⁶ Here we synthesized NUS-8 nanosheets in a bottom-up strategy by performing the reaction in a heterogeneous condition leading to the formation of kinetically favorable intermediate 2D nanosheets. As demonstrated by the field emission scanning electron microscopy (FESEM), transmission electron microscopy (TEM) and atomic force microscopy (AFM) images (Figure 2a,b,e and Figure S1), NUS-8 nanosheets with lateral dimensions of 4–6 μm and thicknesses in the range of 30–50 nm were obtained in circular shape, exhibiting aspect ratios higher than 130. The homogeneity of these nanosheets is confirmed by the statistical analysis on a total of 30 sites (Figure 2g), ruling out the formation of agglomerated nanosheets or isotropic crystals in the final product. The good crystallinity of these nanosheets is clearly evidenced by the selected area electron diffraction (SAED) pattern (inserted in Figure 2c) and ordered lattice structures with a periodic distance of 1.74 nm (Figure 2c,d), corresponding to the (0 0 1) plane of the NUS-8 crystal.¹⁰ Powder X-ray diffraction (PXRD) patterns of NUS-8 nanosheets show the most prominent peak at $2\theta = 5.1^\circ$ ascribing to the diffraction from the (0 0 1) plane (Figure 2h), further proving the preferential orientation of NUS-8 nanosheets along their basal plane. Interestingly, this particular orientation can expose their one-dimensional pores in the direction of gas flux, thus maximizing their separation efficiency inside the composite membranes.¹¹ Permanent porosity of

NUS-8 nanosheets is verified using N_2 sorption isotherms collected at 77 K, in which they exhibit a sharp increase in N_2 uptake at low pressures originating from their good microporosity. Their Brunauer–Emmett–Teller (BET) surface area is $664 \text{ m}^2 \text{ g}^{-1}$ (Figure S2a), much higher than that of other typical MOF nanosheets (e.g., $126 \text{ m}^2 \text{ g}^{-1}$ for Mesh Adjustable Molecular Sieve-1 and $112 \text{ m}^2 \text{ g}^{-1}$ for poly[$Zn_2(\text{benzimidazole})_4$]),^{13,15} highlighting the benefits of using NUS-8 nanosheets as fillers because their high surface area can increase the fractional free volume and provide additional gas adsorption sites in MMMs. Their pore size distribution plots exhibit a maximum value at 5.4 \AA calculated on the basis of nonlocal density functional theory (NLDFT, Figure S2b), matching well with the 6 \AA pore width obtained from their crystal structure model.¹⁰ This pore size is larger than the dynamic diameters of light gases, such as CO_2 (3.3 \AA), N_2 (3.68 \AA), and CH_4 (3.8 \AA), therefore highlighting the rationality of adding NUS-8 in MMMs to construct fast gas permeation highways for the enhancement of gas permeability.

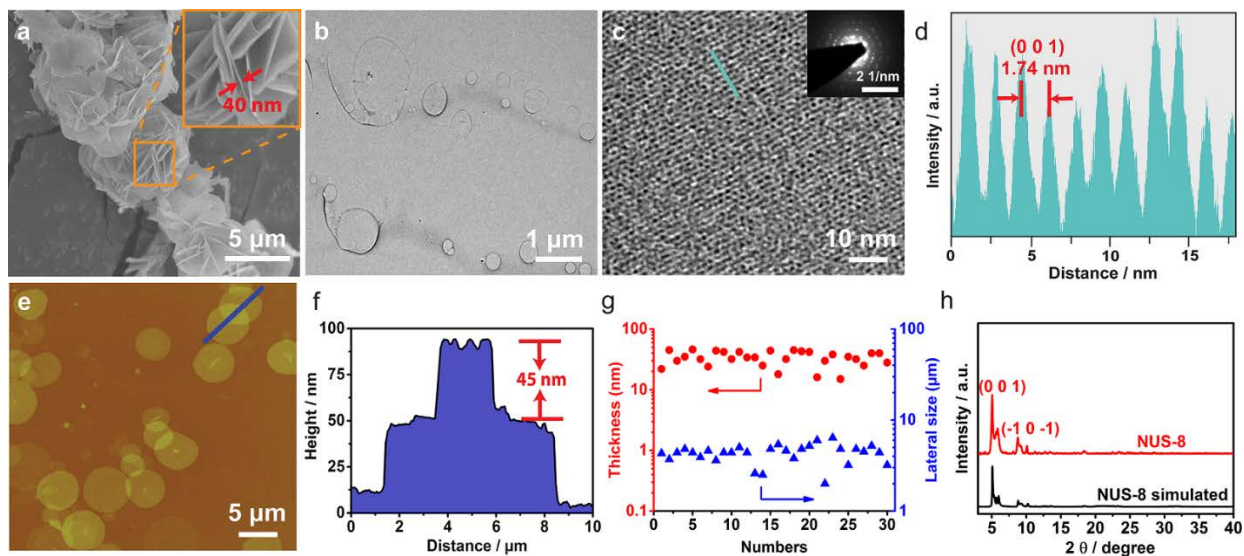


Figure 2. (a) FESEM image of NUS-8 nanosheets synthesized in a bottom-up method. Inset shows the enlargement of these nanosheets. (b) TEM image of NUS-8 nanosheets. (c), (d) High resolution TEM image of NUS-8 nanosheets and their corresponding distance profile, showing periodic lattice structures. Inset in (c) shows their SAED pattern. (e), (f) AFM image of NUS-8 nanosheets

and their corresponding height profile. (g) Static analysis on the thickness and lateral size of NUS-8 nanosheets. (h) PXRD patterns of NUS-8 nanosheets obtained from the experiment and the simulation.

Characterization of membranes

To investigate the optimum NUS-8 loading inside MMMs, a series of NUS-8/PIM-1 MMMs with varied filler loadings, including 0.5, 1, 2 and 5 wt%, were prepared in a conventional solution casting approach and denoted as NUS-8/PIM-1-x, where x represents the weight percentage of fillers inside the membranes. The surface nanostructures and polymer-filler interfacial morphologies of all MMMs were recorded by FESEM (Figure 3a-j). NUS-8 nanosheets are uniformly distributed throughout the PIM-1 matrix, and no sign of microscale polymer-filler phase segregation or filler agglomeration can be observed in all MMMs with the filler loading amount ranging from 0.5–2 wt%. The homogeneous distribution of NUS-8 nanosheets in PIM-1 matrix is clearly evidenced by the EDX mapping analysis (Figure S3). As the loading of NUS-8 nanosheets increases to 5 wt%, aggregated nanosheets with lateral sizes larger than 10 μm were visible in the bottom surface of the MMM (Figure 3e), suggesting that a higher content of nanosheets will not be beneficial for membrane preparation. It is worth mentioning that for conventional three-dimensional isotropic MOF crystals, their optimum filler loading in MMMs usually ranges from 20–50 wt%,¹⁷ which largely surpasses the maximum loading of 5 wt% for NUS-8 nanosheets explored here. This striking difference could be ascribed to the enhanced surface energy of MOF nanosheets that may easily lead to their agglomeration. Similar phenomena have been observed in other 2D materials, such as graphene and MoS₂ nanosheets.¹⁸ Moreover, the addition of NUS-8 nanosheets can induce shear stress around the PIM-1 matrix, leading to the formation of polymer

veins observable in the membrane cross-sectional images (Figure 3g-j).¹⁹ These polymer veins indicate good affinity and strong adhesion between PIM-1 and NUS-8 nanosheets, originating from their high contacting area and favorable interactions in MMMs (*vide infra*).

The thermal stability of pure NUS-8 nanosheets and all membranes was characterized by thermogravimetric analyses (TGA) in air (Figure 3k). Pure NUS-8 nanosheets are thermally stable up to 450 °C, after which they experience a fast weight loss due to the degradation of organic linkers. They complete the weight loss at 550 °C with ZrO₂ as the major residual. On the contrary, pure PIM-1 membrane experiences a gradual thermal degradation starting from 400 °C and its weight loss is completed at 630 °C. Notably, nearly all the hydrocarbons in PIM-1 chains are oxidized into CO₂ and H₂O, leading to a negligible residual weight.²⁰ After the incorporation of NUS-8 nanosheets, all MMMs show enhanced thermal stability and the weight losses are completed at 635, 660, 670, 700 °C for 0.5, 1, 2 and 5 wt% NUS-8/PIM-1 MMMs, respectively. The increased thermal stability of MMMs can be ascribed to the effective hydrogen bonding between hydroxyl groups in NUS-8 nanosheets and cyano groups in PIM-1 backbones, as well as the π - π interactions between abundant benzene rings in both phases.²¹ Fourier transform infrared spectroscopy (FTIR) analysis was performed to further probe the specific interactions in MMMs (Figure S4). The coexistence of O-H bending (1410–1415 cm⁻¹) originating from NUS-8 nanosheets and C-O stretching vibration (1010–1015 cm⁻¹) belonging to PIM-1 contorted backbones in all MMMs indicates the presence of NUS-8 nanosheets inside the PIM-1 matrix. Moreover, the decrease of the intensity of -CN (2230–2240 cm⁻¹) in PIM-1 matrix after the addition of NUS-8 nanosheets confirms the hydrogen bonding between the continuous polymer phase and the dispersed MOF phase.²¹ Generally, this effective hydrogen bonding is supposed to increase the adhesion between these two phases, leading to enhanced mechanical strength of MMMs. To

confirm this hypothesis, nano-indentation measurements were conducted to examine the Young's modulus of all membranes (Figure 3l). It was found that with the incorporation of NUS-8 nanosheets, MMMs exhibit an optimum Young's modulus of 2.82 GPa at 2 wt% filler loading, which is 23.7% higher than that of pure PIM-1 membrane. Nevertheless, at a higher NUS-8 nanosheet loading of 5 wt%, the membrane mechanical strength deteriorates again, as can be expected considering the agglomeration of fillers inside the PIM-1 matrix at this filler loading.

XRD measurements were performed on all membranes to further investigate the packing motif of PIM-1 polymer chains after filler blending (Figure 3m). Pure PIM-1 membrane is amorphous in nature and exhibits two broad peaks at $2\theta = 21.8^\circ$ and 28.5° , corresponding to the chain-chain distances of 4.1 Å and 3.1 Å in the aromatic systems, respectively.¹¹ The characteristic peaks belonging to NUS-8 nanosheets become more prominent in MMMs with the increase of their loading, confirming the maintenance of their good crystallinity during the membrane fabrication owing to their excellent chemical stability (Figure S5).¹⁰ More interestingly, the intensity of the peak located at $2\theta = 28.5^\circ$ becomes even stronger as the filler loading exceeds 2 wt%, illustrating the enhanced PIM-1 matrix crystallinity induced by laminar NUS-8 nanosheets. This indicates a more efficient chain-packing mode with a narrow d-spacing in MMMs that differs from the broad chain distance distribution in pure PIM-1 membrane.

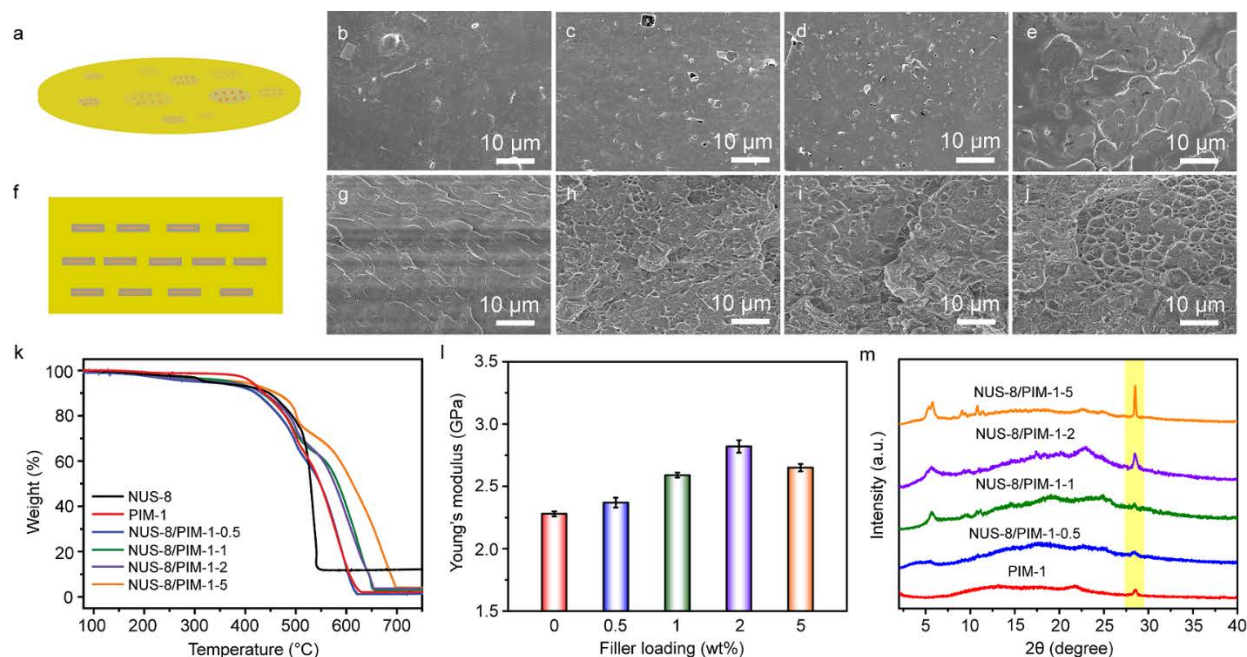


Figure 3 (a), (f) Schematic illustration of the dispersion states of NUS-8 nanosheets in PIM-1 matrix viewed from the membrane bottom surface and cross section. FESEM images of the bottom surface (top row) and the cross section (bottom row) of MMMs with (b), (g) 0.5 wt%; (c), (h) 1 wt%; (d), (i) 2 wt%; and (e), (j) 5 wt% of NUS-8 nanosheets. (k) TGA curves of pure NUS-8, pure PIM-1 membrane and NUS-8/PIM-1 MMMs. (l) Young's modulus of MMMs with various NUS-8 loadings. (m) X-ray diffraction patterns of pure PIM-1 membrane and NUS-8/PIM-1 MMMs.

Considering the strong hydrogen bonding and π - π interactions between NUS-8 nanosheets and the PIM-1 matrix, we speculate that the enhanced PIM-1 crystallinity observed here should originate from the adsorption of PIM-1 chains on the NUS-8 nanosheet surface, which further helps to improve the chain packing efficiency (Figure 4). To validate the adsorption of PIM-1 chains onto NUS-8 nanosheets, measurements on the solution viscosity were performed to directly detect the interactions between the two phases (Figure 5a). Nonporous TiO₂ and microporous UiO-66-NH₂ were chosen as comparisons owing to their unique properties as well as popularities in

MMMs.⁹ The viscosity of pure tetrahydrofuran (THF) is 0.45 mPa·s, which increases to 0.51, 0.54 and 0.62 mPa·s for TiO₂, UiO-66-NH₂ and NUS-8, respectively, after the addition of these fillers into the solvent. The increase in solvent viscosity can be interpreted on the basis of the viscosity theory proposed by Einstein and Smallwood, which illustrates a linear increase of suspension viscosity when increasing solid volume concentration.²² Pure PIM-1 exhibits an intrinsic viscosity of 1.48 mPa·s in THF after stirring for 2 hours, which decreases to 1.43, 1.38 and 1.31 mPa·s after the addition of TiO₂, UiO-66-NH₂ and NUS-8, respectively. More interestingly, the intrinsic viscosity of the solution experiences a further decrease of 5.6% (TiO₂), 23.9% (UiO-66-NH₂) and 35.9% (NUS-8) after stirring for 24 hours. The viscosity decrease in polymer-filler systems can be attributable to one or more of the following three factors: (1) adsorption of polymer chains onto filler surface, reducing the chain entanglement in the bulk solution; (2) extra free volume introduced by fillers; (3) penetration of polymer chains into fillers.²³ The last factor can be ruled out here because the small pore size of fillers (< 6 Å) can block the entering of contorted PIM-1 chains (> 10 Å). Considering the high porosity of UiO-66-NH₂ and NUS-8, they can lead to a more pronounced viscosity decrease compared to nonporous TiO₂. Besides, NUS-8 nanosheets with high aspect ratios can offer more adsorption sites for PIM-1 chains compared to UiO-66-NH₂ nanoparticles (Figure S6), resulting in the largest decrease in the solution viscosity.

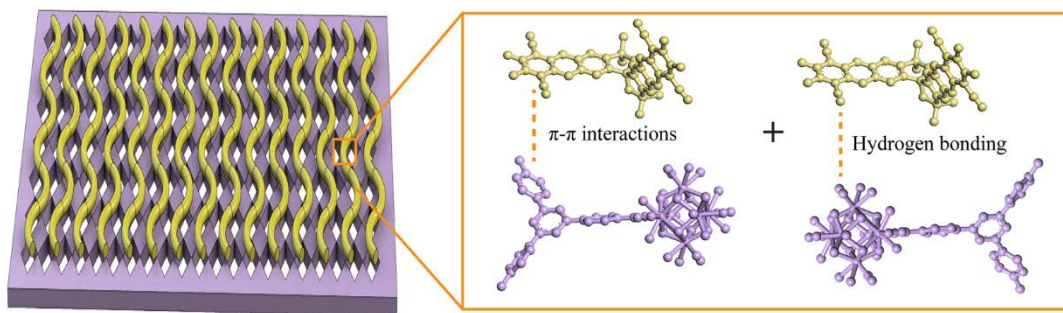


Figure 4. Schematic illustration of the adsorption and alignment of PIM-1 chains on NUS-8 nanosheets owing to their strong π - π interactions and hydrogen bonding.

The more effective chain packing features a narrowed chain packing distance, which can be distinctly evidenced by the positron annihilation lifetime spectroscopy (PALS) measurements. As shown in Figure 5b, pure PIM-1 membrane possesses two dominate free volume diameters centered at 9.75 and 5.18 Å, which shift to 9.45 and 4.83 Å, respectively, after the addition of 2 wt% of NUS-8 nanosheets. This observation differs from the chain packing disruption reported in conventional MMMs containing isotropic MOF nanoparticles,²⁴ while it agrees with polymer chain distance reduction perceived in chemically cross-linking membranes.²⁵ In order to better understand the roles of NUS-8 nanosheets and PIM-1 crystallinity in membrane gas uptake, various gas sorption isotherms (CO₂, CH₄, and N₂) were collected for NUS-8 and membranes at 25 °C (Figure 5c,d, Figure S7). The CO₂ adsorption capacity of NUS-8 could reach 70.8 cm³ g⁻¹ at 1 bar, resulting in the ideal CO₂/CH₄ and CO₂/N₂ adsorption selectivity of 2.48 and 2.62, respectively. The stronger interaction between CO₂ and NUS-8 could be ascribed to the abundant Lewis acidic sites inside the framework, affording higher electrostatic affinities towards CO₂.¹⁰ As for PIM-1 matrix, the polar cyano groups strengthen its interactions with CO₂, and the voids arising from the inefficient chain packing can boost its gas adsorption capacity. Pure PIM-1 membrane exhibits a CO₂ uptake of 37.1 cm³ g⁻¹ at 25 °C up to 1 bar, which is slightly higher than the reported values (27–34 cm³ g⁻¹).²⁶⁻²⁸ Interestingly, the MMM with 2 wt% of NUS-8 shows a CO₂ adsorption capacity of 36.2 cm³ g⁻¹, which is lower than that of each pure phase. The enhanced crystallinity of PIM-1 matrix induced by the addition of 2D NUS-8 nanosheets demonstrates a chain-chain distance of 3.1 Å that is unfavorable for gas uptake, as verified by the reduced CO₂ adsorption capacity in MMMs. This is more prominent for larger molecules, such as N₂ and CH₄, leading to 46.6% and 15.9% increase in the CO₂/CH₄ and CO₂/N₂ adsorption selectivity, respectively, after

the addition of 2 wt% of NUS-8. Therefore, the reduction in polymer chain packing distance will generate more gas discrimination paths within PIM-1 matrix, which will be beneficial for enhancing the membrane gas selectivity.

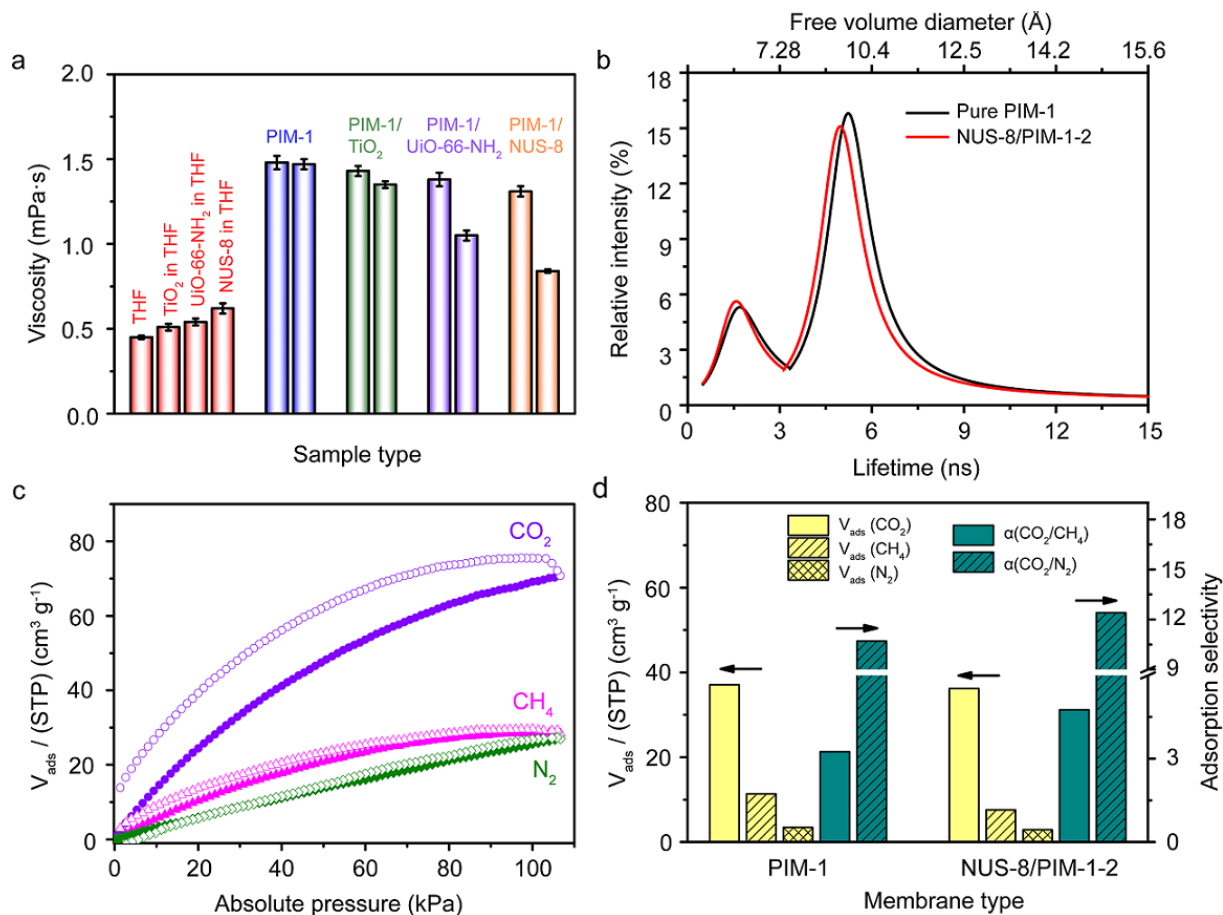


Figure 5. (a) Intrinsic viscosity measurements of pure THF and THF/PIM-1 solutions with various fillers. For THF/PIM-1-filler systems, their viscosities were recorded after 2 h (left) and 24 h (right) stirring. (b) Distribution of ortho-positronium (o-Ps) lifetime and free volume diameter of pure PIM-1 membrane and NUS-8/PIM-1-2 MMM. (c) CO₂, CH₄ and N₂ sorption isotherms collected at 25 °C of NUS-8 nanosheets (filled, adsorption; empty, desorption). (d) CO₂, CH₄ and

N₂ uptake capacity and ideal adsorption selectivity of pure PIM-1 membrane and the MMM with 2 wt% of NUS-8.

Molecular simulations

Molecular simulations integrating density functional theory (DFT) and force field based molecular dynamics (MD) simulations were further performed to shed light on the polymer/MOF interface at the atomistic scale. Full details of the computational strategy are described in the Supporting Information. Figure 6a shows the atomic density profile of the PIM-1/NUS-8 composite as a function of the direction normal to the interface, namely the z coordinate. The NUS-8 model starts at $z = 0$ with the polymer above as shown in Figure 6b. The PIM-1 density fluctuates around a mean-value while away from the MOF, and decays to zero at the proximity of NUS-8. Following our previous work on polymer/MOF interfaces, these two domains can be referred as polymer bulk-like and interfacial regions, respectively.¹² Here, the extension of the domain where PIM-1 and NUS-8 overlap can be defined by the distance separating two limits associated with the non-zero polymer (lower limit) and MOF (upper limit) densities respectively. The corresponding average length of this overlap (3.1 ± 0.6) Å was found to be relatively large, emphasizing a good affinity of the two components. This was also reflected by a homogeneous dispersion of NUS-8 in the PIM-1 matrix experimentally observed. These findings are consistent with the increase of Young's modulus of the MMMs which can be considered as an indication of the good compatibility between PIM-1 and NUS-8, as already reported by Semino et al. for other MOF/polymer composites.¹²

To further examine the interactions between PIM-1 and NUS-8, diverse site-to-site radial distribution functions (RDFs) between the two components of the composite were computed from

the MD simulations and the most representative ones are plotted, as shown in Figure 6c,e. These data evidence that the most significant interactions involve the hydrogen bonding between the cyano groups of PIM-1 and the hydroxyl groups of NUS-8 with a characteristic distance between N (PIM-1) and HOH (NUS-8) of 1.6 Å as assumed above. An illustration of the resultant geometry is provided in Figure 6d. This prediction is fully consistent with the decrease of the FTIR intensity of the -CN groups of PIM-1 in the presence of the NUS-8 nanosheets. Moreover, these simulations evidence that PIM-1 adopts a geometry in such a way to favour π - π interactions between its backbone and the ligands of NUS-8 as revealed by characteristic C(PIM-1)-C(NUS-8) interacting distances in the range of 3.2–4 Å (Figure 6e), corresponding to a parallel orientation of the rings of PIM-1 towards the BTB linker of NUS-8 (Figure 6f). All together these preferential NUS-8/PIM-1 interactions are at the origin of the good adhesion of the two components as experimentally observed.

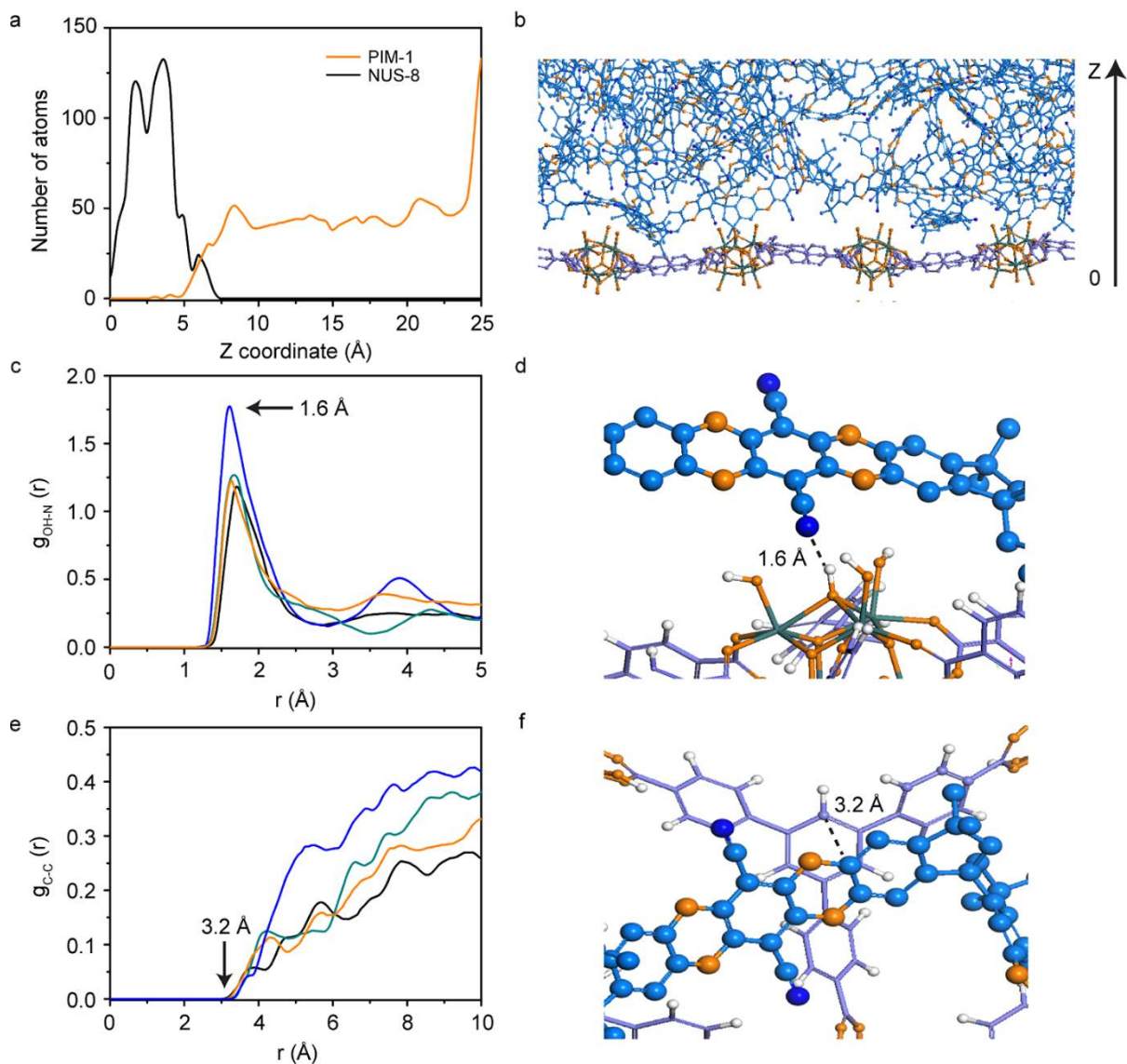


Figure 6. (a) Atomic density profile of PIM-1 (red line) and NUS-8 (black line) along the direction normal to the interface (z-direction). The box represented as dashed lines corresponds to the region of overlap between the MOF and the polymer. (b) Illustration of the PIM-1/NUS-8 interface along the z-direction. (c) Radial distribution functions for the N (PIM-1) and HOH (NUS-8) and (d) illustration for the most preferential MOF/polymer interactions between the nitrile group of PIM-1 and the surface hydroxyl group of NUS-8. (e) Radial distribution functions for the C(PIM-1) and C-(NUS-8) pair and (f) Illustration of the π - π interactions between the backbone of PIM-1 and the

BTB linker of NUS-8. The 4 different plots for the RDFs are extracted from 4 independent MD trajectories performed at 300 K.

Gas separation performance

Gas separation performance of pure PIM-1 membrane and NUS-8/PIM-1 MMMs was evaluated by separating an equimolar mixture of CO₂/CH₄ (natural gas sweetening) or CO₂/N₂ (flue gas purification) in a Wicke-Kallenbach permeation cell (Figure S8) at 25 °C with a transmembrane pressure of 1 bar. As shown in Figure 7a,c, the CO₂ permeability as well as the CO₂/CH₄ and CO₂/N₂ selectivity are strongly related to the loading of NUS-8 nanosheets in the PIM-1 matrix. At low filler loadings (0.5–2 wt%), a simultaneous increase in CO₂ permeability and gas pair selectivity was observed, which excludes the possibility of polymer-filler interfacial defects in MMMs. However, as the NUS-8 nanosheet loading reaches 5 wt%, a sharp decrease in CO₂/CH₄ and CO₂/N₂ selectivity accompanied by a large increase in CO₂ permeability was detected, which is a result of the filler agglomeration-induced nonselective voids in the MMM as described previously. The NUS-8/PIM-1 MMM with 2 wt% of filler loading exhibits the optimum separation performance with a CO₂ permeability of ~6500 Barrer as well as CO₂/CH₄ and CO₂/N₂ selectivities of up to 30.1 and 26.8, respectively. Compared with pure PIM-1 membrane, this MMM exhibits ~65% increase in CO₂ permeability and even larger increase in gas pair selectivity (117% for CO₂/CH₄, 72% for CO₂/N₂), confirming the synergistic effects of porous NUS-8 nanosheets and the PIM-1 matrix with enhanced crystallinity. Specifically, the relatively large pores of the NUS-8 nanosheets provide fast gas diffusion paths inside MMMs, leading to the largely enhanced gas permeability. Similar phenomena have been widely reported in MMMs containing other porous fillers, including SNW-1 (5 Å), UiO-66 (6 Å) and NUS-2 (8 Å).^{19,29,30} For

example, UiO-66 was reported to result in a 72.5% increase in the membrane CO₂ permeability of the MMM with a filler loading of 7.5 wt% compared to the pure polymer membrane.³⁰ Moreover, the enhanced crystallinity in the PIM-1 matrix demonstrates the generation of a more ordered chain packing motif with a chain-chain distance of 3.1 Å in MMMs, which is quite close to the kinetic diameter of CO₂ (3.3 Å). Therefore, the larger molecules, such as N₂ (3.68 Å) and CH₄ (3.8 Å), may experience more resistance compared to CO₂ when diffusing through the orderly packed PIM-1 chains in MMMs, leading to the effective separation based on molecular size differences. This resembles the previous observation that polymer chain rigidification at the polymer-filler interfaces could enhance the membrane gas pair selectivity.^{21,31,32} Nevertheless, in our case, the high aspect ratio of NUS-8 nanosheets and strong polymer-filler interactions could greatly improve the size-sieving capability of the PIM-1 matrix, resulting in higher membrane selectivity increase compared to MMMs containing other porous fillers reported in the literature (Table S5).

The Robeson upper bound plots are widely used for the comparison of various types of membranes (e.g., pure polymeric membranes, MMMs) in terms of their gas permeability and selectivity. As shown in Figure 7b,d, the Robeson 2008 upper bound is surpassed with the incorporation of NUS-8 nanosheets by simultaneously rendering the PIM-1 membrane more permeable and more selective. Especially when compared with commercial polymers, such as polysulfone and cellulose acetate, MMMs reported here show orders of magnitude higher CO₂ permeability while maintaining high CO₂/CH₄ and CO₂/N₂ selectivities. Considering the simplicity of fabricating NUS-8/PIM-1 MMMs by directly adding NUS-8 nanosheets into the PIM-1 matrix, the large-scale production of this type of membranes toward industrial gas separation is very promising in the near future.

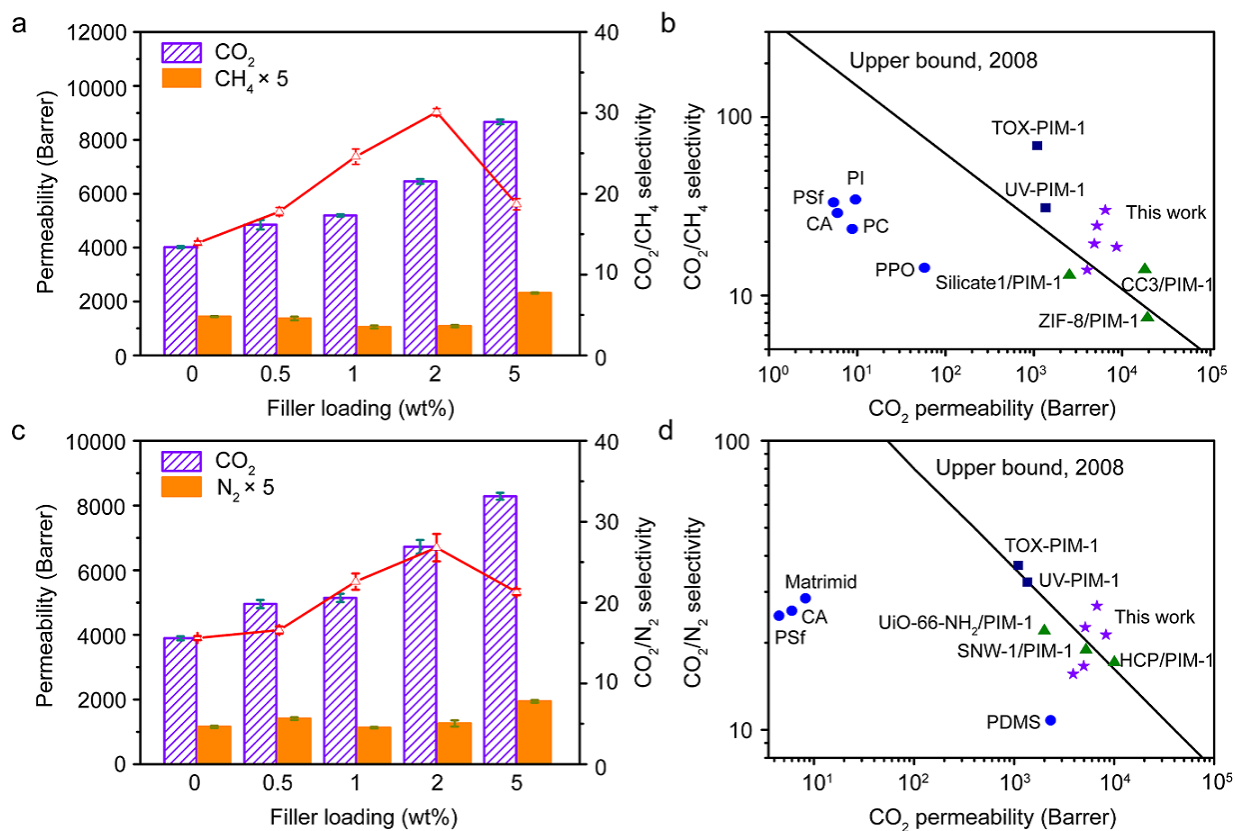


Figure 7. (a) CO₂/CH₄ and (c) CO₂/N₂ separation performance of MMMs with various NUS-8 loadings. Comparison of (b) CO₂/CH₄ and (d) CO₂/N₂ separation performance of as-prepared MMMs with other PIM-1 membranes on 2008 Robeson upper bound plots.

It is of great interest to explore the pressure influence on membrane separation performance, especially in natural gas industry (CO₂/CH₄ separation) where applied high pressures often lead to membrane plasticization. As shown in Figure 8a, pure PIM-1 membrane experiences a 32.7% decrease in CO₂ permeability as the transmembrane pressure increases from 1 bar to 5 bar, accompanied by a 36.6% decrease in CO₂/CH₄ selectivity. This phenomenon can be rationalized by the large decrease in the CO₂ solubility coefficient at high pressures owing to the saturation of Langmuir sites based on dual sorption theory.³³ Specifically, gas sorption in glassy membranes

(e.g., PIM-1) follows the classic dual sorption model that includes the Henry and Langmuir sorption, as shown in Equation (1):

$$C = k_D P + \frac{C'_H b P}{1 + b P} \quad (1)$$

where k_D is the Henry's law constant [$\text{cm}^3(\text{STP}) \text{cm}^{-3}(\text{polymer}) \text{atm}^{-1}$], P refers to the feed pressure (atm), C'_H and b are the Langmuir capacity constant [$\text{cm}^3(\text{STP}) \text{cm}^{-3}(\text{polymer})$] and affinity constant (atm^{-1}), respectively. Gas molecules can be preferentially adsorbed into Langmuir sorption sites over Henry sorption sites at low pressures. Nevertheless, this situation will change owing to the saturation of Langmuir sorption sites at high pressures, leading to the reduction of gas solubility coefficient. Strongly adsorbed gases (e.g., CO_2) possess a greater number of Langmuir sorption sites in glassy membranes compared to weakly adsorbed gases (e.g., CH_4). Therefore, the decrease of gas solubility coefficient is more pronounced for CO_2 compared to CH_4 at high pressures, resulting in the faster decrease of gas permeability for CO_2 over CH_4 and consequently a decreased CO_2/CH_4 selectivity in the membranes at high pressures. However, the MMM with 2 wt% of NUS-8 shows only 11.1% and 8.9% loss in CO_2 permeability and CO_2/CH_4 selectivity, respectively, within the same pressure range. The enhanced capability of preserving good CO_2/CH_4 separation performance for MMMs at high pressures can be explained by the following two reasons. (1) Owing to the strong affinity between NUS-8 and CO_2 as evidenced by the gas adsorption isotherms collected at 25 °C, the added NUS-8 can serve as extra Langmuir sites in MMMs leading to saturation at higher pressures. (2) The enhanced PIM-1 crystallinity in MMMs results in the increase in polymer chain rigidity and the reduction of chain mobility, which can largely suppress the chain swelling effect caused by condensable CO_2 and consequently maintain the excellent CO_2/CH_4 selectivity at high pressures.

Aging is another serious problem in PIM-1 membranes, which illustrates the process of polymer chain relaxation over time. This relaxation process results in the reduction of membrane fractional free volume and the loss of gas permeability.³⁴ As shown in Figure 8b, pure PIM-1 membrane exhibits a loss of CO₂ permeability of up to 35.6% after aging for 120 days, along with a 37.9% increase in CO₂/CH₄ selectivity. This selectivity increase is attributed to the faster collapse process of larger fractional free volume in the membranes, leading to the higher permeability loss of larger gases (e.g. CH₄).³⁵ On the contrary, with the addition of 2 wt% of NUS-8, the resultant MMM shows 22.4% decrease in CO₂ permeability over the same aging period. It is worth mentioning that even after aging for 120 days, the CO₂ permeability of the MMM is still higher than that of pure PIM-1 membrane without aging (5014 Barrer vs. 4020 Barrer), highlighting the importance of gas permeation highways generated by porous NUS-8 fillers for CO₂ transport. The CO₂/CH₄ selectivity increase for the MMM is 18.9%, slightly smaller than that of pure PIM-1 after aging. These results indicate that the coexistence of rigidified polymer chains and porous MOF nanosheets in highly permeable membranes can significantly retard the membrane aging process, opening up their opportunities in industrial gas separation for long-term usage.

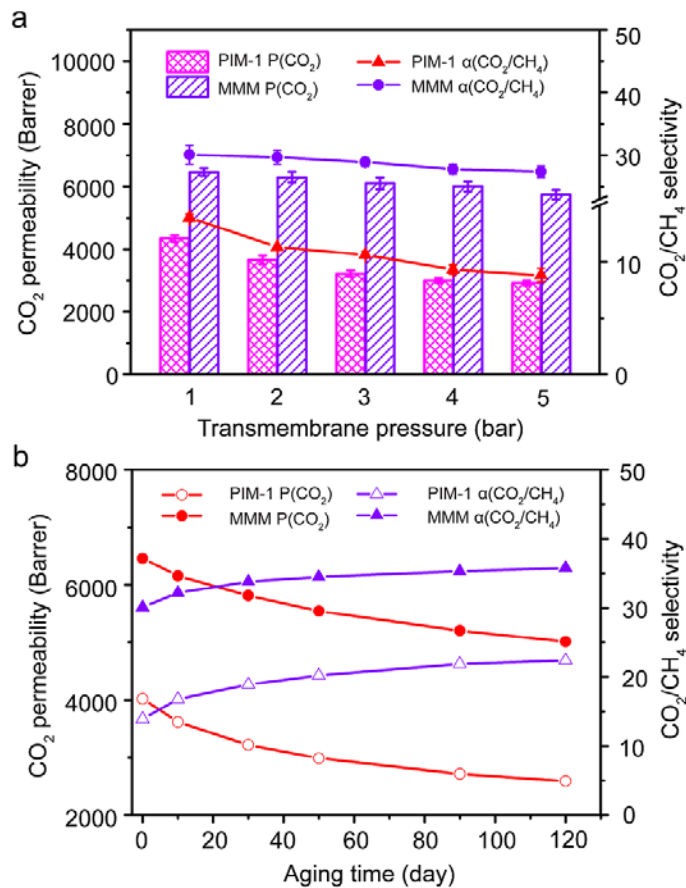


Figure 8. (a) Pressure influence on CO₂/CH₄ separation performance of pure PIM-1 membrane and the NUS-8/PIM-1-2 MMM. (b) Aging behavior of pure PIM-1 membrane and the NUS-8/PIM-1-2 MMM for CO₂/CH₄ separation.

CONCLUSIONS

In summary, we have demonstrated that the incorporation of porous NUS-8 nanosheets into the highly permeable PIM-1 polymer is a novel and highly promising strategy for fabricating high-performance MMMs. The high aspect ratio of NUS-8 nanosheets largely improves their contacting area with PIM-1 polymer chains, leading to the formation of defect-free MMMs. In addition, these nanosheet fillers were designed to possess favorable hydrogen bonding and π - π interactions with

PIM-1 matrix so as to promote the efficient packing of polymer chains. The enhanced PIM-1 crystallinity in MMMs manifests ordered chain-packing motifs with an effective d-spacing of 3.1 Å, which can serve as molecularly discriminative pathways for gas transport. The as-prepared MMMs show high CO₂-selective separation performance, good anti-pressure and anti-aging abilities, which can be attributed to the synergistic interplay between NUS-8 nanosheets and the enhanced crystallinity of PIM-1. This work sheds light on the development of MMMs with great promise in industrial gas separation fields.

ASSOCIATED CONTENT

Supporting Information.

The following files are available free of charge via the Internet at <http://pubs.acs.org>. Additional AFM image, N₂ sorption isotherm, membrane EDX mapping, membrane FTIR spectra, SAXS spectra, FESEM image of UiO-66-NH₂ nanoparticles, membrane gas sorption isotherms for CO₂, CH₄ and N₂ at 25 °C, the scheme of the homo-made membrane testing set up, and gas separation data comparisons. (PDF)

AUTHOR INFORMATION

Corresponding Author

* chezhao@nus.edu.sg

Author Contributions

The manuscript was written through contributions of all authors. All authors have given approval to the final version of the manuscript.

Notes

The authors declare no competing financial interests.

ACKNOWLEDGMENT

This work is supported by National University of Singapore (CENGas R-261-508-001-646), Ministry of Education - Singapore (MOE AcRF Tier 1 R-279-000-472-112, R-279-000-540-114), and Agency for Science, Technology and Research (PSF 1521200078, IRG A1783c0015). C.M.D. is supported by the Australian Research Council (DE140101359). The authors would like to acknowledge the use of Advanced Photon Source, an Office of Science User Facility operated for the U. S. Department of Energy (DOE) Office of Science by Argonne National Laboratory, supported by the U.S. DOE under Contract no. DE-AC02-06CH11357.

REFERENCES

- (1) Scott, V.; Gilfillan, S.; Markusson, N.; Chalmers, H.; Haszeldine, R. S. Last Chance for Carbon Capture and Storage. *Nat. Clim. Change* **2012**, *3*, 105.
- (2) Robeson, L. M. Correlation of Separation Factor versus Permeability for Polymeric Membranes. *J. Membr. Sci.* **1991**, *62*, 165–185.
- (3) Robeson, L. M. The Upper Bound Revisited. *J. Membr. Sci.* **2008**, *320*, 390–400.
- (4) Li, Y.; Chung, T. S.; Kulprathipanja, S. Novel Ag⁺-Zeolite/Polymer Mixed Matrix Membranes with a High CO₂/CH₄ Selectivity. *AIChE J.* **2007**, *53*, 610–616.
- (5) Khan, A. L.; Sree, S. P.; Martens, J. A.; Raza, M. T.; Vankelecom, I. F. J. Mixed Matrix Membranes Comprising of Matrimid and Mesoporous COK-12: Preparation and Gas Separation Properties. *J. Membr. Sci.* **2015**, *495*, 471–478.
- (6) Ameri, E.; Sadeghi, M.; Zarei, N.; Pournaghshband, A. Enhancement of the Gas Separation Properties of Polyurethane Membranes by Alumina Nanoparticles. *J. Membr. Sci.* **2015**, *479*, 11–19.

- (7) Li, X.; Cheng, Y.; Zhang, H.; Wang, S.; Jiang, Z.; Guo, R.; Wu, H. Efficient CO₂ Capture by Functionalized Graphene Oxide Nanosheets as Fillers to Fabricate Multi-Permeable Mixed Matrix Membranes. *ACS Appl. Mater. Interfaces* **2015**, *7*, 5528–5537.
- (8) Liu, G.; Chernikova, V.; Liu, Y.; Zhang, K.; Belmabkhout, Y.; Shekhah, O.; Zhang, C.; Yi, S.; Eddaoudi, M.; Koros, W. J. Mixed Matrix Formulations with MOF Molecular Sieving for Key Energy-Intensive Separations. *Nat. Mater.* **2018**, *17*, 283–289.
- (9) Cheng, Y.; Wang, Z.; Zhao, D. Mixed Matrix Membranes for Natural Gas Upgrading: Current Status and Opportunities. *Ind. Eng. Chem. Res.* **2018**, *57*, 4139–4169.
- (10) Hu, Z.; Mahdi, E. M.; Peng, Y.; Qian, Y.; Zhang, B.; Yan, N.; Yuan, D.; Tan, J.-C.; Zhao, D. Kinetically Controlled Synthesis of Two-Dimensional Zr/Hf Metal–Organic Framework Nanosheets via a Modulated Hydrothermal Approach. *J. Mater. Chem. A* **2017**, *5*, 8954–8963.
- (11) Cheng, Y.; Wang, X.; Jia, C.; Wang, Y.; Zhai, L.; Wang, Q.; Zhao, D. Ultrathin Mixed Matrix Membranes Containing Two-Dimensional Metal–Organic Framework Nanosheets for Efficient CO₂/CH₄ Separation. *J. Membr. Sci.* **2017**, *539*, 213–223.
- (12) Semino, R.; Moreton, J. C.; Ramsahye, N. A.; Cohen, S. M.; Maurin, G. Understanding the Origins of Metal–Organic Framework/Polymer Compatibility. *Chem. Sci.* **2018**, *9*, 315–324.
- (13) Peng, Y.; Li, Y.; Ban, Y.; Jin, H.; Jiao, W.; Liu, X.; Yang, W. Metal–Organic Framework Nanosheets as Building Blocks for Molecular Sieving Membranes. *Science* **2014**, *346*, 1356–1359.
- (14) Li, P.-Z.; Maeda, Y.; Xu, Q. Top-Down Fabrication of Crystalline Metal–Organic Framework Nanosheets. *Chem. Commun.* **2011**, *47*, 8436–8438.
- (15) Wang, X.; Chi, C.; Zhang, K.; Qian, Y.; Gupta, K. M.; Kang, Z.; Jiang, J.; Zhao, D. Reversed Thermo-Switchable Molecular Sieving Membranes Composed of Two-Dimensional Metal–Organic Nanosheets for Gas Separation. *Nat. Commun.* **2017**, *8*, 14460.

- (16) Rodenas, T.; Luz, I.; Prieto, G.; Seoane, B.; Miro, H.; Corma, A.; Kapteijn, F.; Llabrés i Xamena, F. X.; Gascon, J. Metal–Organic Framework Nanosheets in Polymer Composite Materials for Gas Separation. *Nat. Mater.* **2015**, *14*, 48–55.
- (17) Seoane, B.; Coronas, J.; Gascon, I.; Benavides, M. E.; Karvan, O.; Caro, J.; Kapteijn, F.; Gascon, J. Metal–Organic Framework Based Mixed Matrix Membranes: A Solution for Highly Efficient CO₂ Capture? *Chem. Soc. Rev.* **2015**, *44*, 2421–2454.
- (18) Zhu, X.; Tian, C.; Do-Thanh, C.-L.; Dai, S. Two-Dimensional Materials as Prospective Scaffolds for Mixed-Matrix Membrane-Based CO₂ Separation. *ChemSusChem* **2017**, *10*, 3304–3316.
- (19) Kang, Z.; Peng, Y.; Qian, Y.; Yuan, D.; Addicoat, M. A.; Heine, T.; Hu, Z.; Tee, L.; Guo, Z.; Zhao, D. Mixed Matrix Membranes (MMMs) Comprising Exfoliated 2D Covalent Organic Frameworks (COFs) for Efficient CO₂ Separation. *Chem. Mater.* **2016**, *28*, 1277–1285.
- (20) Liao, K. S.; Japip, S.; Lai, J. Y.; Chung, T. S. Boron-Embedded Hydrolyzed PIM-1 Carbon Membranes for Synergistic Ethylene/Ethane Purification. *J. Membr. Sci.* **2017**, *534*, 92–99.
- (21) Ghalei, B.; Sakurai, K.; Kinoshita, Y.; Wakimoto, K.; Isfahani, A. P.; Song, Q.; Doitomi, K.; Furukawa, S.; Hirao, H.; Kusuda, H.; Kitagawa, S.; Sivaniah, E. Enhanced Selectivity in Mixed Matrix Membranes for CO₂ Capture through Efficient Dispersion of Amine-Functionalized MOF Nanoparticles. *Nat. Energy* **2017**, *2*, 17086.
- (22) Mahbubul, I. M.; Saidur, R.; Amalina, M. A. Latest Developments on the Viscosity of Nanofluids. *Int. J. Heat Mass Transf.* **2012**, *55*, 874–885.
- (23) Lau, C. H.; Mulet, X.; Konstas, K.; Doherty, C. M.; Sani, M.-A.; Separovic, F.; Hill, M. R.; Wood, C. D. Hypercrosslinked Additives for Ageless Gas-Separation Membranes. *Angew. Chem. Int. Ed.* **2016**, *128*, 2038–2041.

- (24) Song, Q.; Nataraj, S. K.; Roussenova, M. V.; Tan, J. C.; Hughes, D. J.; Li, W.; Bourgoïn, P.; Alam, M. A.; Cheetham, A. K.; Al-Muhtaseb, S. A.; Sivaniah, E. Zeolitic Imidazolate Framework (ZIF-8) Based Polymer Nanocomposite Membranes for Gas Separation. *Energy Environ. Sci.* **2012**, *5*, 8359–8369.
- (25) Japip, S.; Liao, K. S.; Chung, T. S. Molecularly Tuned Free Volume of Vapor Cross-Linked 6FDA-Durene/ZIF-71 MMMs for H₂/CO₂ Separation at 150 °C. *Adv. Mater.* **2017**, *29*, 1603833.
- (26) Song, Q.; Cao, S.; Zavala-Rivera, P.; Ping Lu, L.; Li, W.; Ji, Y.; Al-Muhtaseb, S. A.; Cheetham, A. K.; Sivaniah, E. Photo-Oxidative Enhancement of Polymeric Molecular Sieve Membranes. *Nat. Commun.* **2013**, *4*, 1918.
- (27) Bushell, A. F.; Attfield, M. P.; Mason, C. R.; Budd, P. M.; Yampolskii, Y.; Starannikova, L.; Rebrov, A.; Bazzarelli, F.; Bernardo, P.; Carolus Jansen, J.; Lanč, M.; Friess, K.; Shantarovich, V.; Gustov, V.; Isaeva, V. Gas Permeation Parameters of Mixed Matrix Membranes Based on the Polymer of Intrinsic Microporosity PIM-1 and the Zeolitic Imidazolate Framework ZIF-8. *J. Membr. Sci.* **2013**, *427*, 48–62.
- (28) Patel, H. A.; Yavuz, C. T. Noninvasive Functionalization of Polymers of Intrinsic Microporosity for Enhanced CO₂ Capture. *Chem. Commun.* **2012**, *48*, 9989–9991.
- (29) Wu, X.; Tian, Z.; Wang, S.; Peng, D.; Yang, L.; Wu, Y.; Xin, Q.; Wu, H.; Jiang, Z. Mixed Matrix Membranes Comprising Polymers of Intrinsic Microporosity and Covalent Organic Framework for Gas Separation. *J. Membr. Sci.* **2017**, *528*, 273–283.
- (30) Shen, J.; Liu, G.; Huang, K.; Li, Q.; Guan, K.; Li, Y.; Jin, W. UiO-66-Polyether Block Amide Mixed Matrix Membranes for CO₂ Separation. *J. Membr. Sci.* **2016**, *513*, 155–165.

- (31) Wu, H.; Li, X.; Li, Y.; Wang, S.; Guo, R.; Jiang, Z.; Wu, C.; Xin, Q.; Lu, X. Facilitated Transport Mixed Matrix Membranes Incorporated with Amine Functionalized MCM-41 for Enhanced Gas Separation Properties. *J. Membr. Sci.* **2014**, *465*, 78–90.
- (32) Li, T.; Pan, Y.; Peinemann, K.-V.; Lai, Z. Carbon Dioxide Selective Mixed Matrix Composite Membrane Containing ZIF-7 Nano-Fillers. *J. Membr. Sci.* **2013**, *425–426*, 235–242.
- (33) Swaidan, R.; Ghanem, B. S.; Litwiller, E.; Pinnau, I. Pure- and Mixed-Gas CO₂/CH₄ Separation Properties of PIM-1 and an Amidoxime-Functionalized PIM-1. *J. Membr. Sci.* **2014**, *457*, 95–102.
- (34) Mitra, T.; Bhavsar, R. S.; Adams, D. J.; Budd, P. M.; Cooper, A. I. PIM-1 Mixed Matrix Membranes for Gas Separations Using Cost-Effective Hypercrosslinked Nanoparticle Fillers. *Chem. Commun.* **2016**, *52*, 5581–5584.
- (35) Lau, C. H.; Konstas, K.; Thornton, A. W.; Liu, A. C. Y.; Mudie, S.; Kennedy, D. F.; Howard, S. C.; Hill, A. J.; Hill, M. R. Gas-Separation Membranes Loaded with Porous Aromatic Frameworks that Improve with Age. *Angew. Chem. Int. Ed.* **2015**, *54*, 2669–2673.

Graphical Abstract

